

Growth and transport properties of Mg_3X_2 ($X = \text{Sb}, \text{Bi}$) single crystals

Jiazhan Xin^{a,b}, Guowei Li^a, Gudrun Auffermann^a, Horst Borrmann^a, Walter Schnelle^a, Johannes Gooth^a, Xinbing Zhao^{b,*}, Tiejun Zhu^{b,*}, Claudia Felser^a, Chenguang Fu^{a,*}

^a Max Planck Institute for Chemical Physics of Solids, Nöthnitzer Str. 40, 01187 Dresden, Germany

^b State Key Laboratory of Silicon Materials, School of Materials Science and Engineering, Zhejiang University, 310027 Hangzhou, China

*Corresponding author.

E-mail addresses: chenguang.fu@cpfs.mpg.de (C.G. Fu); zhaoxb@zju.edu.cn (X.B. Zhao); zhutj@zju.edu.cn (T.J. Zhu)

Abstract

The discovery of high thermoelectric performance in *n*-type polycrystalline $\text{Mg}_3(\text{Sb},\text{Bi})_2$ based Zintl compounds has ignited intensive research interest. However, some fundamental questions concerning the anisotropic transport properties and the origin of intrinsically low thermal conductivity are still elusive, requiring the investigation of single crystals. In this work, high-quality *p*-type Mg_3Sb_2 and Mg_3Bi_2 single crystals have been grown by using a self-flux method. The electrical resistivity ρ of Mg_3Bi_2 single crystal displays an anisotropy with ρ in-plane twice larger than out-of-plane. The low-temperature heat capacity and lattice thermal conductivity of Mg_3Sb_2 and Mg_3Bi_2 single crystals have been investigated by using the Debye-Callaway model, from which the existence of low-lying vibration mode could be concluded. Large Grüneisen parameters and strong anharmonicity are found responsible for the intrinsically low thermal conductivity. Moreover, grain boundary scattering does not contribute significantly to suppress the lattice thermal conductivity of polycrystalline Mg_3Sb_2 . Our results provide insights into the intrinsic transport

properties of Mg_3X_2 and could pave a way to realize enhanced thermoelectric performance in single-crystalline Mg_3X_2 -based Zintl compounds.

Keywords: single crystal growth; thermoelectric properties; Mg_3Sb_2 ; Mg_3Bi_2

1. Introduction

Solid-state thermoelectric (TE) technology, enabling direct and reversible energy conversion between heat and electricity, offers a promising solution for some of today's energy problems and thus, has recently attracted considerable research attention.[1-3] In the past two decades, under tremendous and continuous exploratory efforts, more than ten material systems have been developed as high-performance TE materials with the figure-of-merit zT value exceeding unity, such as bismuth and lead chalcogenides,[4-6] tin selenides,[7,8] copper chalcogenides,[9,10] filled skutterudites,[11-13] half-Heusler alloys,[14-17] and Zintl compounds,[18,19] *etc.* In the perspective of practical application, good TE materials with earth-abundant, low-cost and non-toxic elements are of preference. Among them, Zintl compounds are one of the families possessing these good characteristics. Recently, the surprising discovery of high-performance in *n*-type $\text{Mg}_3(\text{Sb,Bi})_2$ -based Zintl compounds has ignited intensive research activity on this system,[20, 21] especially since almost all the other known Zintl compounds display only good *p*-type TE properties due to their intrinsic point defects.[22, 23]

The Zintl phase Mg_3Sb_2 , which crystalizes in a hexagonal layered structure composed of Mg^{2+} and $(\text{Mg}_2\text{Sb}_2)^{2-}$ layers, was discovered for the first time in 1933.[24] Since the beginning of this century, research attention has been paid to this compound but initial studies only focused on its *p*-type TE properties.[25-27] In 2016, Tamaki *et al.* reported a prominent zT of 1.5 at 716 K in *n*-type $\text{Mg}_{3.2}\text{Sb}_{1.5}\text{Bi}_{0.49}\text{Te}_{0.01}$, and this result has soon been verified by independent groups.[20, 21] Significant features contributing to the excellent TE performance have subsequently been

identified. The multi-valley band behavior combined with light band effective mass, yielding large TE quality factor β , were found to be important reasons underlying the high zT . [21] The diminutive size of Mg in Mg_3Sb_2 , leading to weak interlayer bonding, was attributed to be responsible for its low thermal conductivity. [28] More attempts have been made to further optimize the TE performance of the Mg_3Sb_2 -based compounds, such as proper selection of the dopants on the anion site, [29] rational choice of the alloying compositions (alloyed with Mg_3Bi_2), [30] manipulation of the carrier scattering mechanisms [31, 32] and utilization of the possible anisotropic transport characteristics (forming textures) [33].

The above-mentioned experimental works are all focused on polycrystalline samples while some fundamental questions related to the intrinsic physical properties of this material system are still elusive. For instance, the observed increasing trend of electrical conductivity (σ) with increasing temperature (T) in both p -type and n -type Mg_3Sb_2 at around room temperature was intuitively regarded as the results of ionized impurity scattering on carriers. [20, 34] But it was more recently found that such temperature dependence of carrier mobility (μ) could be altered by enlarging the grain size, indicating that grain boundary scattering might dominate electron transport. [32] Theoretical modeling on the possible grain boundary scattering on carriers was proposed and approximately 60% improvement of zT was predicted at room temperature if grain boundary scattering were eliminated. [35] Furthermore, given the layered structure of $\text{Mg}_3(\text{Sb,Bi})_2$, anisotropic electrical and thermal transport properties are expected. Nevertheless, previous studies did not show obvious anisotropy in transport properties along different directions for the polycrystalline $\text{Mg}_3\text{Sb}_{1.5}\text{Bi}_{0.5}$ synthesized by uniaxial-pressure sintering. [20, 33, 36] To achieve low thermal conductivity (κ) and high zT , previous studies mainly focus on the solid solution composition, while the basic physical properties of the parent compounds are less studied. Interestingly, Mg_3Bi_2 was predicted to be a topological nodal-line semimetal by first-principles calculations and subsequently verified by angle-resolved photoemission spectroscopy. [37, 38] However, the magneto-transport properties of this compound are still missing.

In order to address the above-mentioned questions, it is appealing to grow Mg_3Sb_2 and Mg_3Bi_2 single crystals and to investigate their intrinsic transport properties. In a previous work by Kim *et al.*, $\text{Mg}_3\text{Sb}_{2-x}\text{Bi}_x$ single crystals were grown by using the Bridgman method and the electrical and thermal transport properties below room temperature were reported.[39] Surprisingly, they reported a huge anisotropy in room temperature electrical resistivity ρ of Mg_3Bi_2 single crystal with the out-of-plane ρ 100 times larger than the in-plane ρ . [39] The in-plane room temperature carrier mobility of Mg_3Bi_2 single crystal was reported to be only about $1 \text{ cm}^2\text{V}^{-1}\text{s}^{-1}$. [39] As Mg_3Bi_2 was predicted to be a semimetal, such low carrier mobility in its single crystalline form is unexpected. [30, 40] These contradicting findings also motivate us to reinvestigate the intrinsic transport properties of Mg_3Sb_2 and Mg_3Bi_2 single crystals.

In this work, we have successfully grown Mg_3X_2 ($X = \text{Sb}, \text{Bi}$) single crystals by using a self-flux method. Electrical transport properties measurement shows that the out-of-plane ρ is about half smaller than the in-plane ρ in Mg_3Bi_2 single crystal, which is consistent with the electronic structure calculation showing smaller effective mass along the out-of-plane direction. [17] Near room temperature, the electron transport of Mg_3Bi_2 is dominated by acoustic phonon scattering. Heat capacity and lattice thermal conductivity of Mg_3X_2 single crystals have been investigated by using the Debye-Callaway model. Large Grüneisen parameter and strong anharmonicity are found responsible for the intrinsically low thermal conductivity. Our results provide further insights into the intrinsic transport properties of Mg_3X_2 system.

2. Experimental section

The single crystals of Mg_3Sb_2 and Mg_3Bi_2 were grown by using a self-flux method with Sb or Bi as flux, respectively. Starting elements Mg (granules, 99.8%), Sb (shot, 99.999%) and Bi (shot, 99.999%) were weighed and mixed with molar ratio of Mg: Sb/Bi = 3:7. Tantalum tubes with diameter of 10 mm were used to seal the mixtures in an argon glove box. These Ta tubes were then sealed in quartz tubes under partial

argon pressure. For Mg_3Sb_2 , the ampoule was heated up to 850 °C, kept for 24 hours and then slowly cooled down (2 °C/h) to 630 °C. After that, the ampoule was ramped up to 650 °C and the crystals were separated from the Sb flux through a centrifuging process. It was noted that a thin dense layer of TaSb_2 was formed on the inner surface of the Ta tube during the heating process due to slight reaction between Sb flux and Ta tube.[41] The single crystals of Mg_3Sb_2 tended to “grow” on the TaSb_2 layer, making it easier to separate Mg_3Sb_2 from Sb flux. The obtained single crystals typically had lamellar shape as seen in Fig. S1 with thickness of 0.2 - 1.5 mm, and the flat face was identified as the *ab*-plane with typical length up to 6 - 7 mm. For Mg_3Bi_2 , the mixture was heated up to 650 °C, kept for 24 hours and then slowly cooled down (1.5 °C /h) to 350 °C. Then, the single crystals were separated from the Bi flux through a centrifuging process. Mg_3Bi_2 single crystals exhibit some plasticity compared to the brittle Mg_3Sb_2 single crystals.

The chemical compositions of the single crystals were checked by using a scanning electron microscope (SEM) with an attached energy-dispersive X-ray spectrometer (EDX), which are in agreement with the nominal compositions. The crystals were checked and oriented at room temperature by using a four-circle Rigaku AFC7 X-ray diffractometer with Saturn 724+ CCD detector. Suitable sample edges were selected where transmission of Mo-K_α ($\lambda = 0.71073 \text{ \AA}$) radiation seemed feasible. After successful indexing, oscillation images about the crystallographic axis allowed the assignment of the crystal orientation, confirmed the appropriate choice of the unit cell and showed the excellent crystal quality. The single crystals were then cut along in-plane *b*-axis (010) and out-of-plane *c*-axis (001) directions by using a wire saw for the measurements of anisotropic transport properties. The single crystal nature of the as-cutted Mg_3Sb_2 crystal was further checked by white-beam backscattering Laue X-ray diffraction method. Powder XRD measurements were also performed to check the crystal structure and phase purity, with Cu K_α radiation, and using an image-plate Huber G670 Guinier camera equipped with a Ge (111) monochromator.

Both longitudinal and Hall resistivities of Mg_3Bi_2 single crystals were measured by a standard four-probe method using the AC transport option in a PPMS (Quantum

Design). For Mg_3Sb_2 single crystal, since its resistance is too high, a home-made setup was employed for the electrical transport measurement. As resistivity displays an exponential increase with decreasing temperature, it is difficult to make accurate measurement at low temperature. All contacts were made by using silver-filled paint and 25 μm Platinum wire. To correct for contact misalignment, the measured Hall resistivity was field anti-symmetrized. The Hall coefficient R_H was determined from isothermal magnetic field dependent Hall resistivities (ρ_H). The charge carrier concentration n_H was calculated by $n_H = 1/eR_H$, where e is the unit charge. The thermal conductivity and Seebeck coefficient (S) of Mg_3Bi_2 and Mg_3Sb_2 were measured along b axis by the one-heater and two-thermometer configuration using the thermal transport option (TTO) of the PPMS. The contact was made by using silver-filled epoxy and copper flat wire. The applied temperature gradients were about 1 % of the base temperature. The Seebeck coefficient of Mg_3Sb_2 could not be accurately measured due to extremely high electrical resistance of the sample. The heat capacity (C_p) of Mg_3Sb_2 and Mg_3Bi_2 single crystals was measured from 1.9 K to 320 K by using the heat capacity option of the PPMS.

3. Results and Discussion

The synthesized single crystal of Mg_3Sb_2 displays shiny surface and sharp edges. Clean surface is observed from the SEM image of Mg_3Sb_2 , as displayed in Fig. 1a. Powder XRD pattern of Mg_3Sb_2 shows no obvious impurity phase (Fig. S2, Supporting Information SI), indicating good phase purity of the single crystal. For Mg_3Bi_2 , large surfaces of the crystal are clean and flat, but some remaining Bi flux on the sample surface is also found in the SEM image (Fig. 1d). The reflection pattern of Bi is also detectable in the powder XRD pattern of Mg_3Bi_2 (Fig. S2b), which is probably due to the inadequate centrifuging process. Thus, before performing the transport measurement, the crystal was well polished to remove the Bi flux. The calculated lattice parameters of both crystals are shown in Fig. S2 and are in agreement with the literature data.[42, 43] Furthermore, single crystal XRD

diffraction images of Mg_3Sb_2 and Mg_3Bi_2 along b and c directions respectively are shown in Fig. 1(b-c, e-f). Sharp and distinct spots are observed, which indicates good quality of the crystals. The faint powder rings in Fig. 1e-f are probably attributed to the slight distortions or powder contaminations on the surface. More information about single crystal XRD results can be found in Fig. S3-S4. Laue diffraction pattern of Mg_3Sb_2 crystal is further shown in Fig. S5.

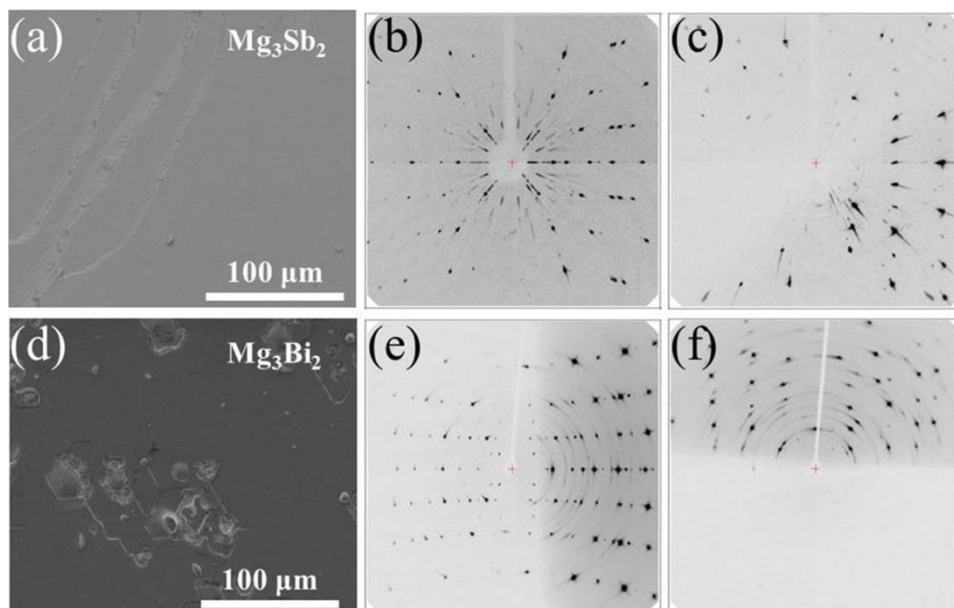


Fig. 1. SEM and single crystal diffraction images for selected crystals of Mg_3Sb_2 (a - c) and Mg_3Bi_2 (d - f). (b) and (e) are reflecting oscillations about b -axis, (c) and (f) about c -axis. Reflection broadening is due to surface distortion induced by sample preparation.

Mg_3X_2 crystallize in the hexagonal anti- La_2O_3 structure type with a cationic Mg^{2+} sheet and an anionic $[\text{Mg}_2\text{X}_2]^{2-}$ layer stack along the c axis (Fig. 2a). This layered structure raises the question whether the electrical and thermal transport properties of $\text{Mg}_3(\text{Sb,Bi})_2$ are anisotropic, *i.e.*, different for in-plane (ab plane) and out-of-plane (c axis) directions. Tamaki *et al.* calculated the sound velocities of the longitudinal acoustic mode of Mg_3Sb_2 along ΓM direction (in-plane) and ΓA (out-of-plane) and they found similar values along these two directions and thus, concluded that the thermal conduction should be isotropic.[20] The electronic structure of Mg_3X_2 has been calculated by Zhang *et al.*, whose results show that the Fermi surfaces in conduction band minimum are approximately spherical while in valence band maximum the in-plane effective mass is about 10 times larger than the out-of-plane

one, indicating isotropic and anisotropic electrical transport properties in n -type and p -type Mg_3X_2 , respectively.[21] In experiments, the TE properties of n -type polycrystalline $\text{Mg}_3(\text{Sb,Bi})_2$ along directions parallel and perpendicular to the pressing direction was reported, showing no obvious difference.[33]

To give our answer to the question of anisotropy, we measured the temperature-dependent electrical resistivity of the Mg_3Bi_2 and Mg_3Sb_2 single crystals along the in-plane b axis and the out-of-plane c axis, respectively. As both crystals were grown in the Mg-poor chemical environment, they exhibit p -type conducting behavior. The results, which would reflect the anisotropy of the valence band, are displayed in Fig. 2b and 2c. Distinct from the previous report by Kim *et al.*, who found a huge anisotropy in Mg_3Bi_2 with the out-of-plane resistivity 100 times larger than the in-plane resistivity,[39] our results show the resistivity along out-of-plane c axis is approximately half of that along in-plane b axis in the whole investigated temperature range. While both Kim's and our crystals display positive Seebeck coefficient (seen in Fig. S6), indicating the electrical transport is dominated by holes, the huge difference in the anisotropy is confusing. Recalling the electronic structure calculation by Zhang *et al.*,[21] showing lower valence band effective mass along c axis, our finding of lower resistivity along c axis is in qualitative agreement with the expecting result from band structure. The resistivity of Mg_3Sb_2 is about 6 orders of magnitude higher than that of Mg_3Bi_2 and shows typical semiconducting behavior, which indicates that the Fermi level should lie in the forbidden gap. The anisotropic resistivity is more complicated. As shown in Fig. 2c, ρ_c is smaller than ρ_b at around room temperature, whereas ρ_c becomes larger than ρ_b below 255K. Thus, the difference in ρ_c and ρ_b of Mg_3Sb_2 might not give accurate information concerning the anisotropy of electrical transport properties.

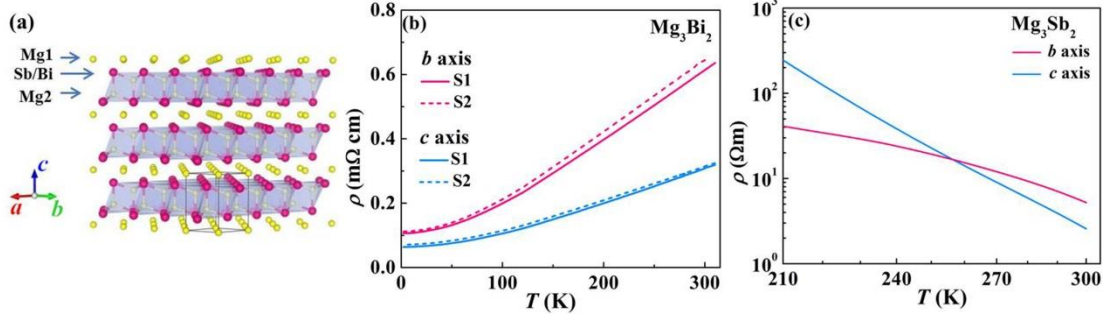


Fig. 2. (a) Crystal structure of Mg₃Bi₂ and Mg₃Sb₂ (drawn using VESTA)[44]; Temperature dependent electrical resistivity of (b) Mg₃Bi₂ and (c) Mg₃Sb₂ single crystals along in-plane *b* axis and out-of-plane *c* axis, respectively. To confirm the result of anisotropic resistivity, two different Mg₃Bi₂ single crystals, denoted as S1 and S2 respectively, were selected from the same batch for the measurement, which give consistent results.

Mg₃Bi₂ was predicted to be a topological type-II nodal-line semimetal by first-principles calculations and subsequently verified by angle-resolved photoemission spectroscopy, but its magneto-transport properties were not reported yet.[37, 38] Many discovered topological semimetals show large magnetoresistance (MR) and high carrier mobility, which motivates us to investigate the MR of Mg₃Bi₂ single crystal. As shown in Fig. 3a, the MR displays a nearly linear behavior with the increase of magnetic field in the investigated temperature range. A maximum MR of 3% is obtained at 2 K and 9 T, which however, is much smaller than that of other topological semimetals, such as the Dirac semimetals Cd₃As₂ and PtSn₄[45, 46] or the Weyl semimetals NbP and TaAs.[47-49] To explore the possible reason leading to this low MR, we further measured the Hall resistivity ρ_H of Mg₃Bi₂, as shown in Fig. 3b. The $\rho_H(H)$ shows a positive and linear increase with magnetic field, indicating that the electrical transport properties is dominated by holes. The Hall carrier concentration is further calculated by the slope of $\rho_H(H)$, as displayed in Fig. 3c. A slight increase in n_H with rising temperature is found and the $n_H(T)$ at room temperature is about $2.5 \times 10^{20} \text{ cm}^{-3}$. The calculated carrier mobility $\mu_H(T)$ decreases with rising temperature. Especially above 100 K, $\mu_H(T)$ follows a T^{-1} relationship, which is a typical behavior for heavily doped semiconductors or metals when the acoustic phonon scattering dominates the electron transport. $\mu_H(T)$ of Mg₃Bi₂ at 2 K is

around several hundreds of $\text{cm}^2\text{V}^{-1}\text{s}^{-1}$, which is much smaller than that of the other topological semimetals. For example, the carrier mobility of NbP single crystal at 2 K is almost 4 orders of magnitude higher than that of Mg_3Bi_2 . [47] Thus, the low carrier mobility could be the one of the reasons why Mg_3Bi_2 has much lower MR compared to other topological semimetals.

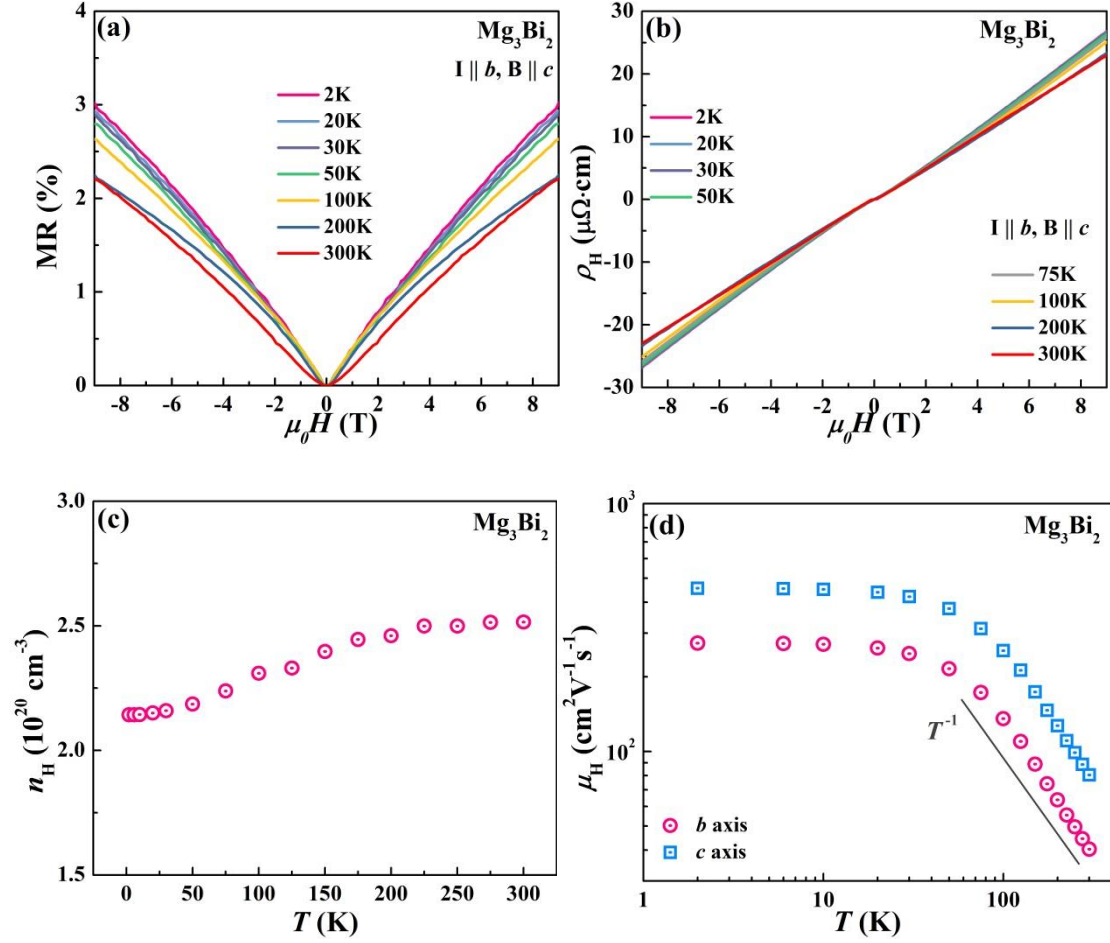


Fig. 3. (a) Magnetoresistance (MR) and (b) Hall resistivity of the Mg_3Bi_2 single crystal at different temperatures measured in magnetic fields up to 9 T. The electrical current was applied along b axis and the magnetic field along c axis. (c) Temperature-dependent Hall carrier concentration n_H and (d) carrier mobility μ_H . The positive slope of Hall resistivity indicates p -type conducting behavior.

The thermal conductivity and lattice thermal conductivity of single crystalline Mg_3Sb_2 and Mg_3Bi_2 along b axis are shown in Fig. 4. The lattice thermal conductivity of Mg_3Bi_2 was calculated by subtracting the electronic term κ_e which was determined

according to the Wiedemann–Franz law, $\kappa_e = L\sigma T$, using the temperature dependent Lorenz number L , which was roughly calculated from the Seebeck coefficient based on a single parabolic band model.[50] The lattice thermal conductivity of Mg_3Sb_2 is almost the same with its thermal conductivity due to its extremely high electrical resistivity and thus negligible electronic thermal conductivity. The lattice thermal conductivity of both Mg_3Sb_2 and Mg_3Bi_2 exhibits normal temperature dependency, in which κ_L first increases with increasing temperature, reaches its peak value at around $\theta_D/20$ (θ_D is 241 K and 175 K respectively, as shown below), and then decreases at higher temperature. Above 20 K, the $\kappa_L(T)$ of Mg_3Sb_2 exhibits a nearly T^{-1} relationship due the dominant phonon-phonon Umklapp scattering.

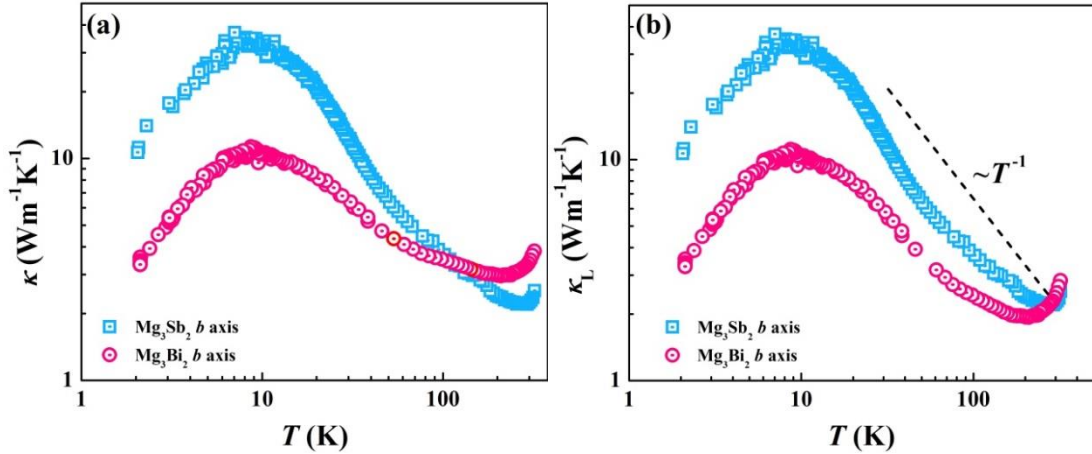
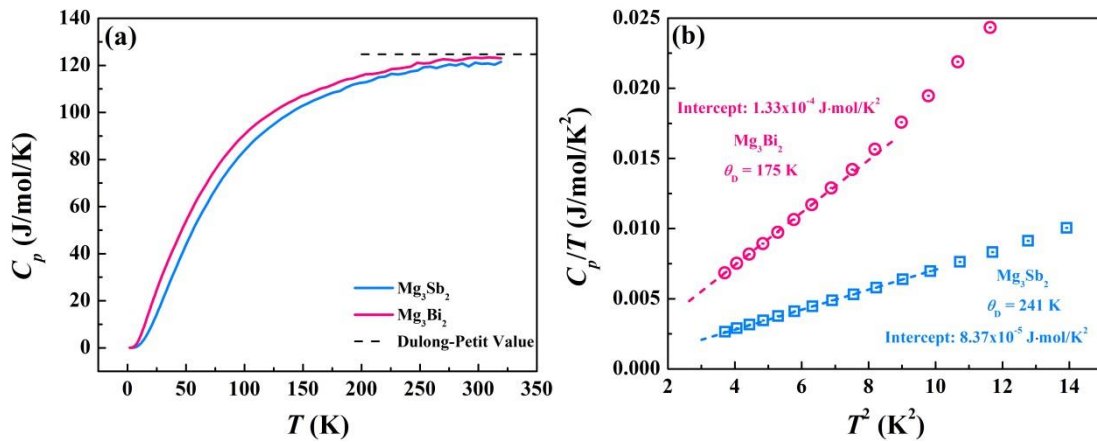


Fig. 4. Temperature dependences of (a) thermal conductivity and (b) lattice thermal conductivity of the Mg_3Sb_2 and Mg_3Bi_2 single crystals along b axis.

One interesting question is why Mg_3Sb_2 and Mg_3Bi_2 have lower κ_L compared to the other isostructural AMg_2X_2 ($A = \text{Mg}, \text{Ca}, \text{and Yb}$) Zintl compounds like CaMg_2Sb_2 and CaMg_2Bi_2 . This issue has recently been discussed by Peng *et al.*[28] They proposed that the diminutive size of Mg^{2+} leads to low-lying transverse phonon modes and large mode Grüneisen parameters, which thus contribute to the inherently low κ_L of Mg_3X_2 . To check for the existence of low-lying vibration modes,[28] the low-temperature heat capacity of both Mg_3Sb_2 and Mg_3Bi_2 was further measured and is shown in Fig. 5a. As only the low frequency phonons could be excited at $T \ll \theta_D/10$ (long wave length limit), the C_p at that temperatures would obey the Debye T^3

law as seen in Fig. 5b. Therefore, the Debye temperatures of these two compounds were calculated by using equation $C_p/T = \delta + 2.4\pi^4 n N_A k_B \theta_D^{-3} T^2$, where δ is a constant from the contribution of electrons, N_A is the Avogadro constant, n is the number of atoms per primitive cell, k_B is the Boltzmann constant.[51] The calculated θ_D (241 K for Mg_3Sb_2 and 175 K for Mg_3Bi_2) is in accordance with the values obtained from theoretical calculations (238 K for Mg_3Sb_2 and 177 K for Mg_3Bi_2).[52] At higher temperature, the experimental C_p gradually exhibits deviation from the calculated C_p if only based on the Debye T^3 approximation, as seen in Fig. 5b. Considering the possible existence of low-lying vibration modes, the Debye-Einstein model, in which additional Einstein oscillators are included, was used to fit the experimental C_p . The additional Einstein term is expressed as $C_p = A_i(\theta_{Ei})^2 T^{-3} (e^{\theta_{Ei}/T}) / (e^{\theta_{Ei}/T} - 1)^2$, where θ_{Ei} is the Einstein temperature for the i^{th} Einstein oscillator and A_i is the fitting parameter (detailed calculation can be found in SI).[53] As seen in Fig. 5c and 5d, one Einstein oscillator is necessary to fit the experimental C_p , with Einstein temperature θ_{E1} of 64 K for Mg_3Sb_2 and 44 K for Mg_3Bi_2 . The corresponding frequency of the Einstein oscillator for Mg_3Sb_2 and Mg_3Bi_2 is 44.2 cm^{-1} and 30.8 cm^{-1} . The derived low-lying vibration mode in Mg_3Sb_2 is qualitatively agreeing with the calculation by Peng et al.,[28] showing a low-lying transverse phonon mode with similar frequency and very large Grüneisen parameter at A point of the Brillouin zone. Thus, we could conclude that the existence of low-lying vibration mode in Mg_3X_2 system.



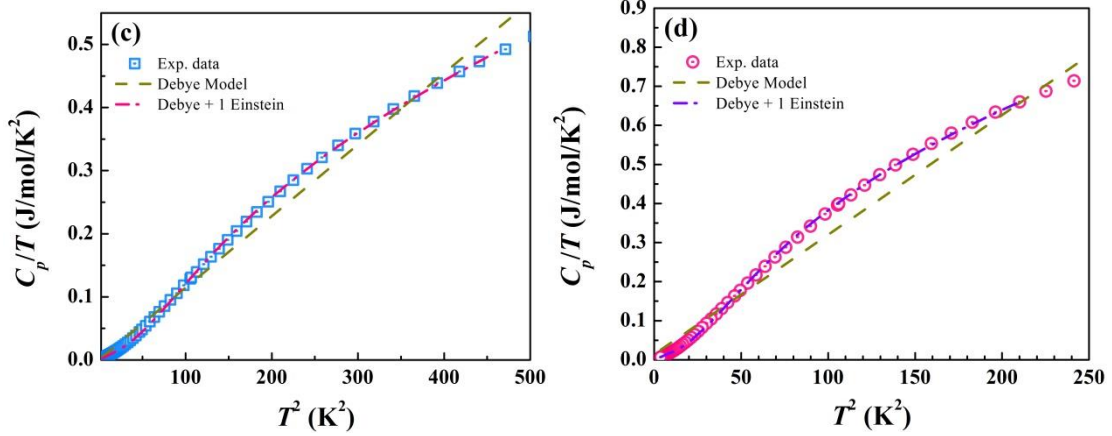


Fig. 5. Temperature dependence of specific heat capacity of Mg_3Sb_2 and Mg_3Bi_2 single crystals, presented as (a) C_p versus T and (b-d) C_p/T versus T^2 , together with the calculated curves based on Debye-Einstein model (more detailed fitting results could be seen in Fig. S7).

The above analysis of low-temperature C_p shows the existence of low-lying vibration mode, and then it is interesting to quantitatively estimate its influence on the κ_L of Mg_3Sb_2 and Mg_3Bi_2 . Herein, the low-lying vibration mode is taken as resonant scattering term, as the other researchers did for the other TE materials.[53, 54] The modified Debye-Callaway model [55] was used to fit the experimental κ_L , with phonon-phonon scattering (U and N), boundary scattering (B), point defect scattering (PD), resonant scattering (PR) taken into consideration (calculation details seen in SI). The resonant frequency used in calculating the scattering rate of resonant scattering was derived from the fitting results of low temperature specific heat capacity. As seen in Fig. 6, the experimental κ_L is in agreement with the theoretical fit by introducing all the scattering processes mentioned above. It is found that the low-lying vibration mode and the induced phonon resonant scattering have strong influence on the κ_L within the low temperature region, which is similar to the cases in α - MgAgSb and filled skutterudites.[53, 56] Furthermore, the Grüneisen parameters for longitude and transverse phonon branches (γ_L and γ_T) used to fit the experimental data are extremely large ($\gamma_L = 4.33$, $\gamma_T = 2.22$ for Mg_3Sb_2 and $\gamma_L = 6.49$, $\gamma_T = 2.22$ for Mg_3Bi_2), which is in accordance with the calculated large mode Grüneisen parameters by Peng *et al.*[28] Therefore, we conclude that the large Grüneisen parameter and the strong anharmonicity are the origin of the intrinsically low thermal conductivity of Mg_3X_2 .

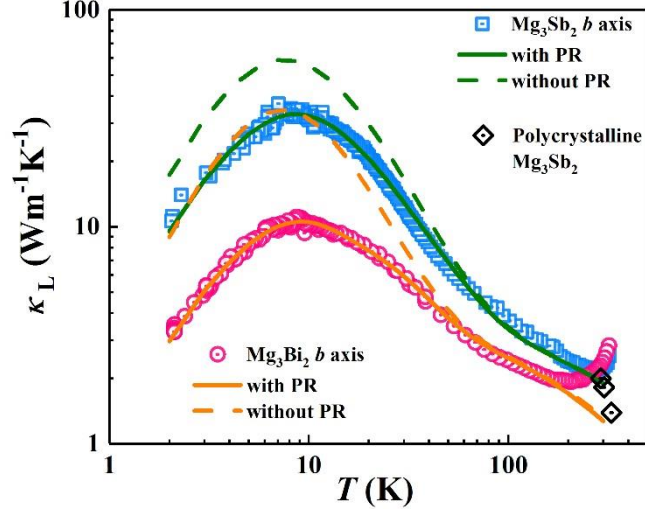


Fig.6 Temperature dependence of lattice thermal conductivity of single crystalline Mg_3Sb_2 and Mg_3Bi_2 . The solid and dash curves are calculated based on the modified Debye-Callaway model with and without resonant scattering (PR), respectively. The data of polycrystalline Mg_3Sb_2 are taken from the references.[20, 26, 34]

As a further discussion, it is worth to roughly estimate the TE performance of single crystalline Mg_3X_2 system. The room temperature κ_L of polycrystalline Mg_3Sb_2 as shown in Fig. 6,[20, 26, 34] is only about 15% lower than that of the single crystalline Mg_3Sb_2 . This surprisingly small difference in κ_L between polycrystalline and single crystalline Mg_3Sb_2 indicates that grain boundary scattering does not contribute significantly to further suppress the lattice thermal conductivity of polycrystalline samples. In contrast, since the electron mobility could be largely improved by eliminating the grain boundary, which has been justified in previous work,[32, 35] one can optimistically expect higher TE performance in *n*-type single crystalline Mg_3X_2 system.

4. Conclusions

In summary, single crystals of Mg_3Sb_2 and Mg_3Bi_2 have been successfully grown by using the self-flux method. In the Mg-poor synthesis environment, all the obtained single crystals exhibit *p*-type transport properties, of which the Mg_3Sb_2 shows typical semiconducting behavior and the Mg_3Bi_2 shows semimetal behavior. We found that the electrical resistivity of Mg_3Bi_2 single crystal displays an obvious anisotropy with

the out-of-plane resistivity about half of the in-plane resistivity. Magnetoresistance of Mg_3Bi_2 was measured, which shows a maximum value of 3% at 2 K and 9 T. The low-temperature heat capacity and lattice thermal conductivity of Mg_3Sb_2 and Mg_3Bi_2 single crystals have been investigated based on the modified Debye-Callaway model, which justifies the existence of low-lying vibration mode. Large Grüneisen parameters and strong anharmonicity were found responsible for the intrinsically low thermal conductivity. Moreover, the lattice thermal conductivity of single crystalline Mg_3Sb_2 is only about 15% higher than that of the polycrystalline samples, indicating higher TE performance might be achieved in *n*-type single crystalline Mg_3X_2 system as the carrier mobility can be significantly enhanced.

Acknowledgements

This work was financially supported by the ERC Advanced Grant No. (742068) “TOP-MAT” and funded by the Deutsche Forschungsgemeinschaft (DFG, German Research Foundation) – Projektnummer (392228380). C. G. Fu acknowledges the financial support from Alexander von Humboldt Foundation. The authors thank Jiong Yang from Shanghai University for helpful discussion.

References

- [1] G. J. Snyder and E. S. Toberer, Complex thermoelectric materials, *Nat. Mater.* 7 (2008) 105-114.
- [2] T. Zhu, Y. Liu, C. Fu, J. P. Heremans, J. G. Snyder and X. Zhao, Compromise and Synergy in High-Efficiency Thermoelectric Materials, *Adv. Mater.* 29 (2017) 1605884.
- [3] W. Liu, J. Hu, S. Zhang, M. Deng, C-G Han, and Y. Liu, New trends, strategies and opportunities in thermoelectric materials: A perspective, *Mater. Today Phys.* 1 (2017) 50-60.
- [4] B. Poudel, Q. Hao, Y. Ma, Y. Lan, A. Minnich, B. Yu, X. Yan, D. Wang, A. Muto, D. Vashaee, X. Chen, J. Liu, M. S. Dresselhaus, G. Chen and Z. Ren, High-Thermoelectric Performance of Nanostructured Bismuth Antimony Telluride Bulk Alloys, *Science* 320 (2008) 634-638.
- [5] Y. Pei, X. Shi, A. LaLonde, H. Wang, L. Chen and G. J. Snyder, Convergence of electronic bands for high performance bulk thermoelectrics, *Nature* 473 (2011) 66-69.

- [6] K. Biswas, J. He, I. D. Blum, C. I. Wu, T. P. Hogan, D. N. Seidman, V. P. Dravid and M. G. Kanatzidis, High-performance bulk thermoelectrics with all-scale hierarchical architectures, *Nature* 489 (2012) 414-418.
- [7] L.-D. Zhao, G. Tan, S. Hao, J. He, Y. Pei, H. Chi, H. Wang, S. Gong, H. Xu and V. P. Dravid, Ultrahigh power factor and thermoelectric performance in hole-doped single-crystal SnSe, *Science* 351 (2015) 141-144.
- [8] Y. Wu, W. Li, A. Faghaninia, Z. Chen, J. Li, X. Zhang, B. Gao, S. Lin, B. Zhou, A. Jain, Y. Pei, *Mater. Today Phys.* 3 (2017) 127-136.
- [9] H. Liu, X. Shi, F. Xu, L. Zhang, W. Zhang, L. Chen, Q. Li, C. Uher, T. Day and G. J. Snyder, Copper ion liquid-like thermoelectrics, *Nat. Mater.* 11 (2012) 422-425.
- [10] S. D. Kang, J.-H. Pöhls, U. Aydemir, P. Qiu, C. C. Stoumpos, R. Hanus, M. A. White, X. Shi, L. Chen, M. G. Kanatzidis and G. J. Snyder, Enhanced stability and thermoelectric figure-of-merit in copper selenide by lithium doping, *Mater. Today Phys.* 1 (2017) 7-13.
- [11] X. Shi, J. Yang, J. R. Salvador, M. Chi, J. Y. Cho, H. Wang, S. Bai, J. Yang, W. Zhang and L. Chen, Multiple-Filled Skutterudites: High Thermoelectric Figure of Merit through Separately Optimizing Electrical and Thermal Transports, *J. Am. Chem. Soc.* 133 (2011) 7837-7846.
- [12] Y. Tang, Z. M. Gibbs, L. A. Agapito, G. Li, H.-S. Kim, M. B. Nardelli, S. Curtarolo and G. J. Snyder, Convergence of multi-valley bands as the electronic origin of high thermoelectric performance in CoSb₃ skutterudites, *Nat. Mater.* 14 (2015) 1223-1228.
- [13] W. Zhao, Z. Liu, Z. Sun, Q. Zhang, P. Wei, X. Mu, H. Zhou, C. Li, S. Ma, D. He, P. Ji, W. Zhu, X. Nie, X. Su, X. Tang, B. Shen, X. Dong, J. Yang, Y. Liu and J. Shi, Superparamagnetic enhancement of thermoelectric performance, *Nature* 549 (2017) 247-251.
- [14] C. Fu, S. Bai, Y. Liu, Y. Tang, L. Chen, X. Zhao and T. Zhu, Realizing high figure of merit in heavy-band p-type half-Heusler thermoelectric materials, *Nat. Commun.* 6 (2015) 8144.
- [15] H. Zhu, R. He, J. Mao, Q. Zhu, C. Li, J. Sun, W. Ren, Y. Wang, Z. Liu, Z. Tang, A. Sotnikov, Z. Wang, D. Broido, D. J. Singh, G. Chen, K. Nielsch and Z. Ren, Discovery of ZrCoBi based half Heuslers with high thermoelectric conversion efficiency, *Nat. Commun.* 9 (2018) 2497.
- [16] R. He, H. Zhu, J. Sun, J. Mao, H. Reith, S. Chen, G. Schierning, K. Nielsch and Z. Ren, Improved thermoelectric performance of n-type half-Heusler MCo_{1-x}Ni_xSb (M = Hf, Zr), *Mater. Today Phys.* 1 (2017) 24-30.
- [17] Y. Liu, C. Fu, K. Xia, J. Yu, X. Zhao, H. Pan, C. Felser and T. Zhu, Lanthanide Contraction as a Design Factor for High-Performance Half-Heusler Thermoelectric Materials, *Adv. Mater.* 30 (2018) 1800881.
- [18] J. Shuai, J. Mao, S. Song, Q. Zhang, G. Chen and Z. Ren, Recent progress and future challenges on thermoelectric Zintl materials, *Mater. Today Phys.* 1 (2017) 74-95.
- [19] S. M. Kauzlarich, S. R. Brown and G. Jeffrey Snyder, Zintl phases for thermoelectric devices, *Dalton Trans.* (2007) 2099-2107.

- [20] H. Tamaki, H. K. Sato and T. Kanno, Isotropic Conduction Network and Defect Chemistry in $\text{Mg}_{3+\delta}\text{Sb}_2$ -Based Layered Zintl Compounds with High Thermoelectric Performance, *Adv. Mater.* 28 (2016) 10182-10187.
- [21] J. Zhang, L. Song, S. H. Pedersen, H. Yin, L. T. Hung and B. B. Iversen, Discovery of high-performance low-cost n-type Mg_3Sb_2 -based thermoelectric materials with multi-valley conduction bands, *Nat. Commun.* 8 (2017) 13901.
- [22] J. Shuai, H. Geng, Y. Lan, Z. Zhu, C. Wang, Z. Liu, J. Bao, C. W. Chu, J. Sui and Z. Ren, Higher thermoelectric performance of Zintl phases $(\text{Eu}_{0.5}\text{Yb}_{0.5})_{1-x}\text{Ca}_x\text{Mg}_2\text{Bi}_2$ by band engineering and strain fluctuation, *Proc. Natl. Acad. Sci. USA* 113 (2016) E4125-32.
- [23] J. Zhang, L. Song, G. K. H. Madsen, K. F. F. Fischer, W. Zhang, X. Shi and B. B. Iversen, Designing high-performance layered thermoelectric materials through orbital engineering, *Nat. Commun.* 7 (2016) 10892.
- [24] E. Zintl and E. Husemann. Bindungsart und Gitterbau binärer Magnesiumverbindungen. *Zeitschrift für Physikalische Chemie* 21B (1933) 138.
- [25] T. Kajikawa, N. Kimura and T. Yokoyama. Thermoelectric properties of intermetallic compounds: Mg_3Bi_2 and Mg_3Sb_2 for medium temperature range thermoelectric elements. *Thermoelectrics, 2003 Twenty-Second International Conference on - ICT*, (2003) 305-308.
- [26] C. L. Condon, S. M. Kauzlarich, F. Gascoin and G. J. Snyder, Thermoelectric properties and microstructure of Mg_3Sb_2 , *J. Solid State Chem.* 179 (2006) 2252-2257.
- [27] A. Bhardwaj, N. S. Chauhan and D. K. Misra, Significantly enhanced thermoelectric figure of merit of p-type Mg_3Sb_2 -based Zintl phase compounds via nanostructuring and employing high energy mechanical milling coupled with spark plasma sintering, *J. Mater. Chem. A* 3 (2015) 10777-10786.
- [28] W. Peng, G. Petretto, G.-M. Rignanese, G. Hautier and A. Zevalkin, An Unlikely Route to Low Lattice Thermal Conductivity: Small Atoms in a Simple Layered Structure, *Joule* 2 (2018) 1879-1893.
- [29] J. Zhang, L. Song, K. A. Borup, M. R. V. Jørgensen and B. B. Iversen, New Insight on Tuning Electrical Transport Properties via Chalcogen Doping in n-type Mg_3Sb_2 -Based Thermoelectric Materials, *Adv. Energy Mater.* 8 (2018) 1702776.
- [30] K. Imasato, S. D. Kang, S. Ohno and G. J. Snyder, Band engineering in Mg_3Sb_2 by alloying with Mg_3Bi_2 for enhanced thermoelectric performance, *Mater. Horiz.* 5 (2018) 59-64.
- [31] J. Mao, J. Shuai, S. Song, Y. Wu, R. Dally, J. Zhou, Z. Liu, J. Sun, Q. Zhang, C. dela Cruz, S. Wilson, Y. Pei, D. J. Singh, G. Chen, C.-W. Chu and Z. Ren, Manipulation of ionized impurity scattering for achieving high thermoelectric performance in n-type Mg_3Sb_2 -based materials, *Proc. Natl. Acad. Sci.* 114 (2017) 10548-10553.
- [32] T. Kanno, H. Tamaki, H. K. Sato, S. D. Kang, S. Ohno, K. Imasato, J. J. Kuo, G. J. Snyder and Y. Miyazaki, Enhancement of average thermoelectric figure of merit by increasing the grain-size of $\text{Mg}_{3.2}\text{Sb}_{1.5}\text{Bi}_{0.49}\text{Te}_{0.01}$, *Appl. Phys. Lett.* 112 (2018) 033903.

- [33] S. Song, J. Mao, J. Shuai, H. Zhu, Z. Ren, U. Saparamadu, Z. Tang, B. Wang and Z. Ren, Study on anisotropy of n-type Mg_3Sb_2 -based thermoelectric materials, *Appl. Phys. Lett.* 112 (2018) 092103.
- [34] Z. Ren, J. Shuai, J. Mao, Q. Zhu, S. Song, Y. Ni and S. Chen, Significantly enhanced thermoelectric properties of p-type Mg_3Sb_2 via co-doping of Na and Zn, *Acta Mater.* 143 (2018) 265-271.
- [35] J. J. Kuo, S. D. Kang, K. Imasato, H. Tamaki, S. Ohno, T. Kanno and G. J. Snyder, Grain boundary dominated charge transport in Mg_3Sb_2 -based compounds, *Energy Environ. Sci.* 11 (2018) 429-434.
- [36] A. Bhardwaj and D. K. Misra, Enhancing thermoelectric properties of a p-type Mg_3Sb_2 -based Zintl phase compound by Pb substitution in the anionic framework, *RSC Adv.* 4 (2014) 34552-34560.
- [37] X. Zhang, L. Jin, X. Dai and G. Liu, Topological Type-II Nodal Line Semimetal and Dirac Semimetal State in Stable Kagome Compound Mg_3Bi_2 , *J. Phys. Chem. Lett.* 8 (2017) 4814-4819.
- [38] T.-R. Chang, I. Pletikovic, T. Kong, G. Bian, A. Huang, J. Denlinger, S. K. Kushwaha, B. Sinkovic, H.-T. Jeng and T. Valla, Realization of a Type-II Nodal-Line Semimetal in Mg_3Bi_2 , arXiv:1711.09167 (2017).
- [39] S. H. Kim, C. M. Kim, Y.-K. Hong, K. I. Sim, J. H. Kim, T. Onimaru, T. Takabatake and M.-H. Jung, Thermoelectric properties of $\text{Mg}_3\text{Sb}_{2-x}\text{Bi}_x$ single crystals grown by Bridgman method, *Mater. Res. Express* 2 (2015) 055903.
- [40] L. M. Watson, C. A. W. Marshall and C. P. Cardoso, On the electronic structure of the semiconducting compounds Mg_3Bi_2 and Mg_3Sb_2 , *J. Phys. F: Met. Phys.* 14 (1984) 113-121.
- [41] F. Failamani, P. Broz, D. Macciò, S. Puchegger, H. Müller, L. Salamakha, H. Michor, A. Grytsiv, A. Saccone, E. Bauer, G. Giester and P. Rogl, Constitution of the systems $\{\text{V}, \text{Nb}, \text{Ta}\}$ -Sb and physical properties of di-antimonides $\{\text{V}, \text{Nb}, \text{Ta}\}\text{Sb}_2$, *Intermet.* 65 (2015) 94-110.
- [42] M. Martinez-Ripoll, A. Haase and G. Brauer, The crystal structure of α - Mg_3Sb_2 , *Acta Crystallogr. Sect. B* 30 (1974) 2006-2009.
- [43] V. B. Lazarev, S. F. Marenkin, V. Y. Shevchenko and G. I. Goncharenko, Preparation of Mg_3Bi_2 and some of its semiconductive properties, *Neorganicheskie Materialy* 10 (1974) 1882-1883.
- [44] K. Momma and F. Izumi, VESTA 3 for three-dimensional visualization of crystal, volumetric and morphology data, *J. Appl. Crystallogr.* 44 (2011) 1272-1276.
- [45] T. Liang, Q. Gibson, M. N. Ali, M. Liu, R. J. Cava and N. P. Ong, Ultrahigh mobility and giant magnetoresistance in the Dirac semimetal Cd_3As_2 , *Nat. Mater.* 14 (2015) 280-284.
- [46] C. Fu, T. Scaffidi, J. Waissman, Y. Sun, R. Saha, S. J. Watzman, A. K. Srivastava, G. Li, W. Schnelle, P. Werner, M. E. Kamminga, S. Sachdev, S. S. P. Parkin, S. A. Hartoll, C. Felser, and J. Gooth, Thermoelectric signatures of the electron-phonon fluid in PtSn_4 , arXiv:1802.09468 (2018).
- [47] C. Shekhar, A. K. Nayak, Y. Sun, M. Schmidt, M. Nicklas, I. Leermakers, U. Zeitler, Y. Skourski, J. Wosnitza, Z. Liu, Y. Chen, W. Schnelle, H. Borrmann, Y.

Grin, C. Felser and B. Yan, Extremely large magnetoresistance and ultrahigh mobility in the topological Weyl semimetal candidate NbP, *Nat. Phys.* 11 (2015) 645-649.

[48]L. X. Yang, Z. K. Liu, Y. Sun, H. Peng, H. F. Yang, T. Zhang, B. Zhou, Y. Zhang, Y. F. Guo, M. Rahn, D. Prabhakaran, Z. Hussain, S. K. Mo, C. Felser, B. Yan and Y. L. Chen, Weyl semimetal phase in the non-centrosymmetric compound TaAs, *Nat. Phys.* 11 (2015) 728-732.

[49]C. Fu, S. N. Guin, S. J. Watzman, G. Li, E. Liu, N. Kumar, V. Süß, W. Schnelle, G. Auffermann, C. Shekhar, Y. Sun, J. Gooth and C. Felser, Large Nernst power factor over a broad temperature range in polycrystalline Weyl semimetal NbP, *Energy Environ. Sci.* (2018). DOI: 10.1039/C8EE02077A

[50]A. May and G. Snyder, Introduction to Modeling Thermoelectric Transport at High Temperatures, in: D. M. Rowe (Ed.), *Materials, Preparation, and Characterization in Thermoelectrics*, CRC Press, Boca Raton, 2012, pp. 1-18.

[51]C. Kittel. *Introduction to solid state physics*, Wiley New York, 2005.

[52]A. Jain, S. P. Ong, G. Hautier, W. Chen, W. D. Richards, S. Dacek, S. Cholia, D. Gunter, D. Skinner, G. Ceder and K. A. Persson, Commentary: The Materials Project: A materials genome approach to accelerating materials innovation, *APL Materials* 1 (2013) 011002.

[53]P. Ying, X. Li, Y. Wang, J. Yang, C. Fu, W. Zhang, X. Zhao and T. Zhu, Hierarchical Chemical Bonds Contributing to the Intrinsically Low Thermal Conductivity in α -MgAgSb Thermoelectric Materials, *Adv. Funct. Mater.* 27 (2017) 1604145.

[54]W. Qiu, L. Xi, P. Wei, X. Ke, J. Yang and W. Zhang, Part-crystalline part-liquid state and rattling-like thermal damping in materials with chemical-bond hierarchy, *Proc. Natl. Acad. Sci.* 111 (2014) 15031-15035.

[55]D. T. Morelli, J. P. Heremans and G. A. Slack, Estimation of the isotope effect on the lattice thermal conductivity of group IV and group III-V semiconductors, *Phys. Rev. B* 66 (2002) 195304.

[56]J. Yang, D. T. Morelli, G. P. Meisner, W. Chen, J. S. Dyck and C. Uher, Effect of Sn substituting for Sb on the low-temperature transport properties of ytterbium-filled skutterudites, *Phys. Rev. B* 67 (2003) 165207.

Supporting Information

Growth and transport properties of Mg_3X_2 ($X = \text{Sb}, \text{Bi}$) single crystals

Jiazhan Xin^{a,b}, Guowei Li^a, Gudrun Auffermann^a, Horst Borrmann^a, Walter Schnelle^a, Johannes Gooth^a, Xinbing Zhao^{b,*}, Tiejun Zhu^{b,*}, Claudia Felser^a, Chenguang Fu^{a,*}

^a Max Planck Institute for Chemical Physics of Solids, Nöthnitzer Str. 40, 01187 Dresden, Germany

^b State Key Laboratory of Silicon Materials, School of Materials Science and Engineering, Zhejiang University, 310027 Hangzhou, China

*Corresponding author.

E-mail: chenguang.fu@cpfs.mpg.de (C. G. Fu); zhaoxb@zju.edu.cn (X. B. Zhao); zhutj@zju.edu.cn (T. J. Zhu)

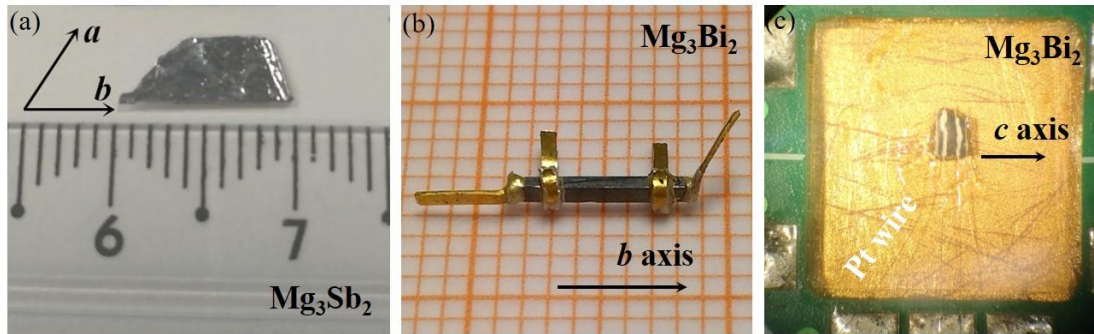


Fig. S1. Optical images of the single crystals of (a) Mg_3Sb_2 and (b, c) Mg_3Bi_2 . (b) Four copper leads were used for thermal transport measurement. (c) A typical four-probe electrical resistivity measurement setup for Mg_3Bi_2 crystal along c -axis with the length of about 0.6 mm.

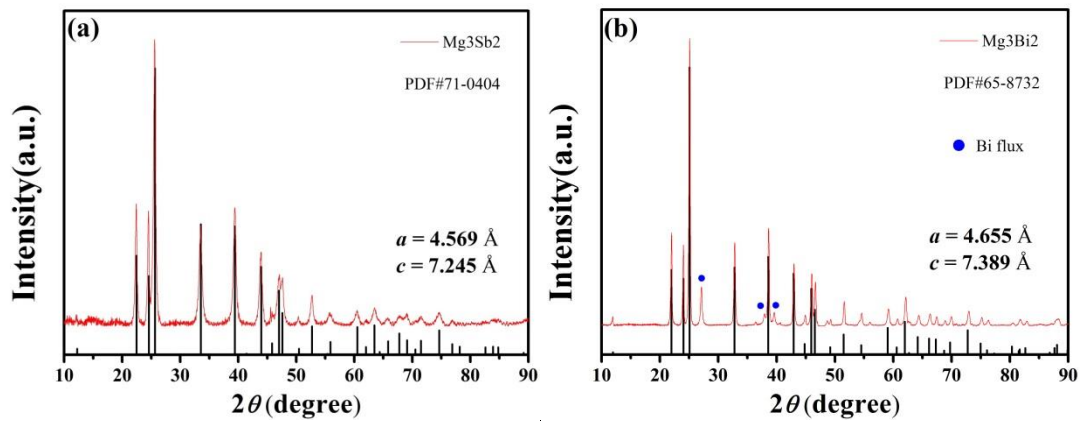


Fig. S2. Powder XRD results of (a) Mg_3Sb_2 and (b) Mg_3Bi_2 .

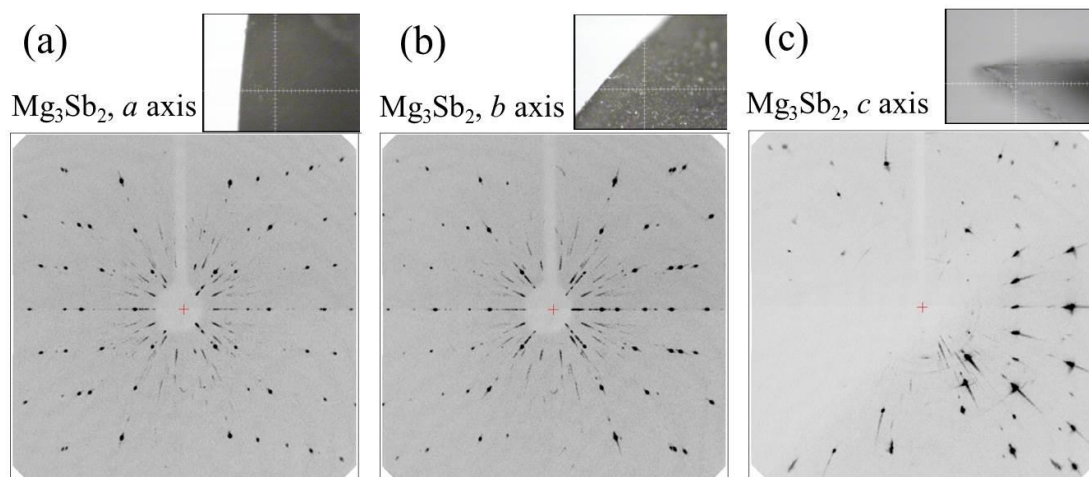


Fig. S3. Single crystal XRD results of Mg_3Sb_2 ; the patterns were obtained with the X-ray along (a) a axis, (b) b axis and (c) c axis.

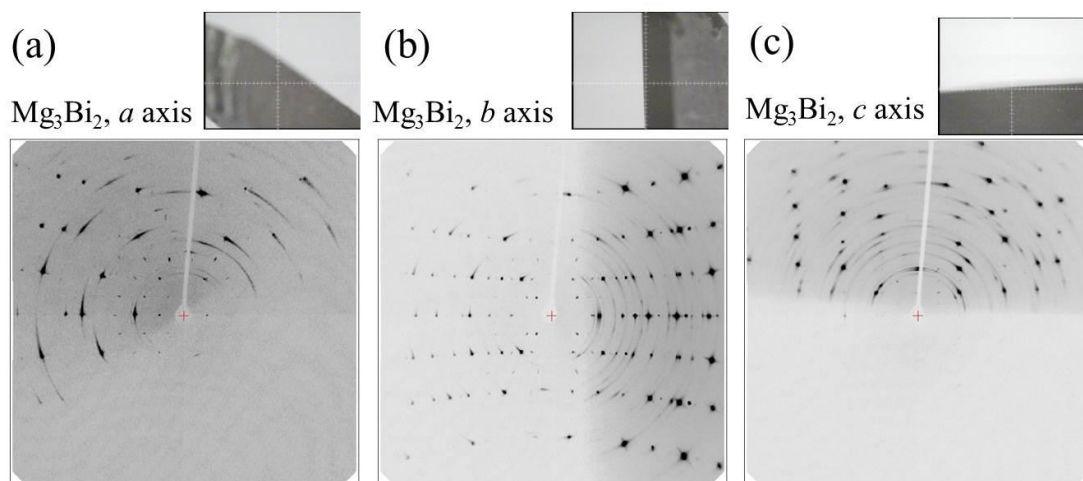


Fig. S4. Single crystal XRD results of Mg_3Bi_2 ; the patterns were obtained with the X-ray along (a) a axis, (b) b axis and (c) c axis.

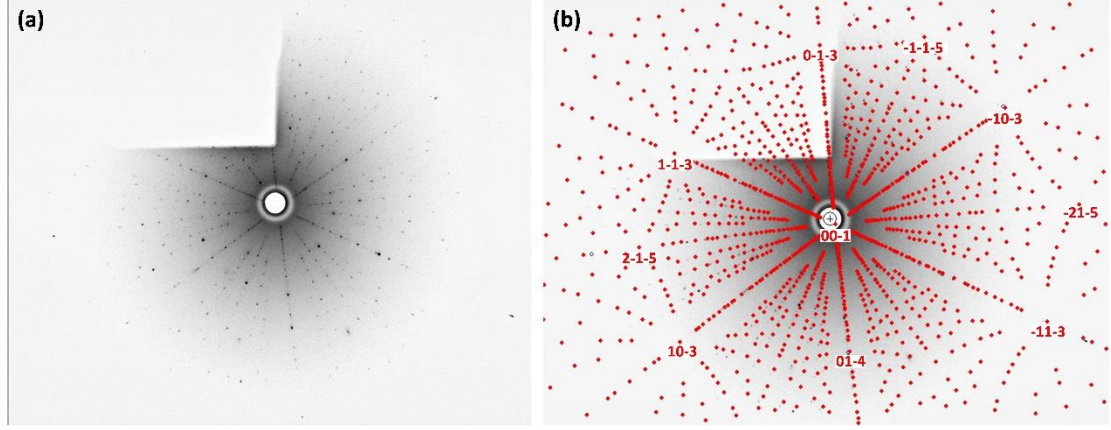


Fig. S5. (a) Laue diffraction pattern of the Mg_3Sb_2 single crystal. (b) The diffraction pattern can be indexed based on $P\bar{3}m1$ space group, as superposed with a theoretically simulated pattern. The corresponding diffraction spots locate exactly up to the indices.

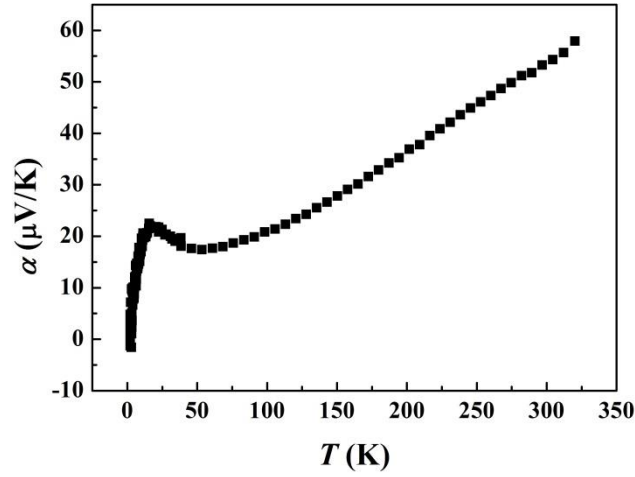


Fig. S6. Temperature dependence of Seebeck coefficient for the Mg_3Bi_2 single crystal along b axis.

Modeling analysis for C_p

The low temperature specific heat capacity C_p was fitted by using the Debye-Einstein model:[1]

$$C_p = \delta T + 9N_A k_B \left(\frac{T}{\theta_D}\right)^3 \int_0^{x_D} \frac{x^4 e^x}{(e^x - 1)^2} dx + \sum_{i=1}^n A_i (\theta_{E_i})^2 (T^2)^{-\frac{3}{2}} \frac{e^{\frac{\theta_{E_i}}{T}}}{\left(e^{\frac{\theta_{E_i}}{T}} - 1\right)^2},$$

$$x = \hbar\omega/k_B T \quad (S1)$$

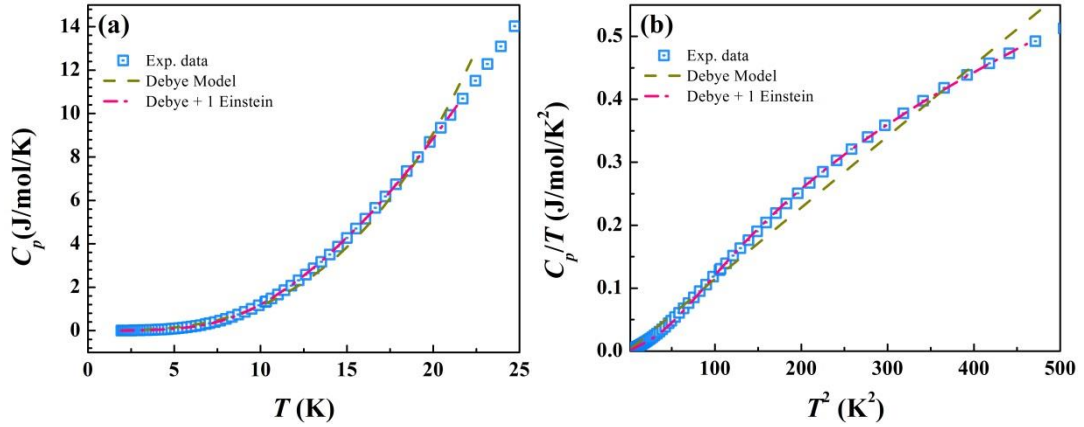
Where δT denotes the heat capacity contributed by electrons, the second term denotes the part described by the Debye model of specific heat capacity and the third term denotes the total contributions of each Einstein oscillators with Einstein temperature, θ_{Ei} (n is the number of the Einstein oscillators). And δ , Debye temperature θ_D , and A_i are the fitting parameters.

As the Einstein terms of heat capacity has little influence at very low temperature ($T \leq \theta_D/10$) and the Debye terms could be simplified into the well-known T^3 relation, C_v has the form:

$$C_p = \delta T + \frac{12}{5} \pi^4 n N_A k_B \left(\frac{T}{\theta_D}\right)^3 \quad (S2)$$

By fitting experimental data below certain temperatures ($T^2 < 10 \text{ K}^2$ for Mg_3Bi_2 and $T^2 < 20 \text{ K}^2$ for Mg_3Sb_2), δ and θ_D were obtained.

Then, Einstein terms were added to fit the data with broader temperature range. It was found that one Einstein oscillators are adequate to realize good fits with the experimental data. All the above mentioned fitting parameters and fitting results could be seen in Table S1 and Fig. S7.



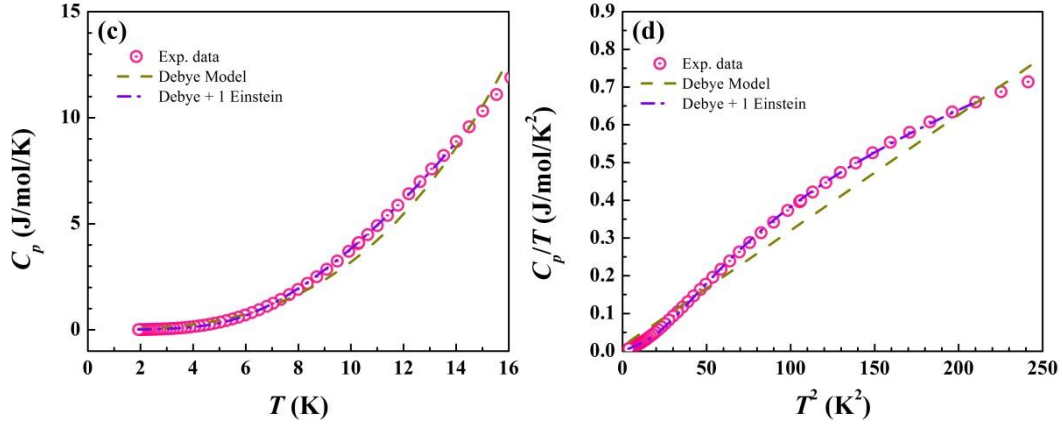


Fig. S7. Temperature dependence of specific heat capacity of (a, b) Mg_3Sb_2 and (c, d) Mg_3Bi_2 .

Table S1. Fitting parameters for the specific heat capacity

	δ (mJ/mol/K ²)	θ_D (K)	A_1 (J/mol/K)	θ_{E1} (K)	f_{E1} (cm ⁻¹)
Mg₃Sb₂	0.084	241	7.31	64	44.2
Mg₃Bi₂	0.133	175	8.43	44	30.8

Thermal conductivity analysis based on the modified Debye-Callaway model

The experimental lattice thermal conductivity of the single crystals were analyzed by using the modified Debye-Callaway model proposed by Morelli *et al.*, [2] in which longitude and transverse acoustic phonon modes are calculated individually and the fitting parameters for Normal and Umklapp process are transformed to the Grüneisen parameters of each phonon modes. Calculation details go as follows.

The lattice thermal conductivity κ is expressed as

$$\kappa = \kappa_L + 2\kappa_T \quad (\text{S3})$$

where κ_L and κ_T are the lattice thermal conductivity contributed by longitude and transverse acoustic phonon modes respectively. And thermal conductivity of each modes could be expressed as a uniform expression: [3, 4]

$$\kappa_i = \kappa_{i1} + \kappa_{i2}, (i = L, T) \quad (S4)$$

where κ_{i1} represents the overall thermal conductivity for the longitude or transverse mode considering all the scattering process, and κ_{i2} could be understood as a correction term due to the non-resistive three phonon Normal process (N). And κ_{i1} and κ_{i2} could be expressed as:

$$\kappa_{i1} = \frac{1}{3} C_i T^3 \int_0^{\theta_i/T} \frac{\tau_C^i x^4 e^x}{(e^x - 1)^2} dx \quad (S5a)$$

$$\kappa_{i2} = \frac{1}{3} C_i T^3 \frac{\left[\int_0^{\theta_i/T} \frac{\tau_C^i x^4 e^x}{\tau_N^i (e^x - 1)^2} dx \right]^2}{\int_0^{\theta_i/T} \frac{\tau_C^i x^4 e^x}{\tau_N^i \tau_R^i (e^x - 1)^2} dx}, \quad C_i = \frac{k_B^4}{2\pi^2 \hbar^3 v_i} \quad (S5b)$$

Where $x = \hbar\omega/k_B T$ is the reduced phonon energy, \hbar is the reduced Planck constant, k_B is the Boltzmann constant, ω is the phonon frequency, θ_i and v_i are the Debye temperature and the sound velocity for specific phonon mode, τ_c^i is the combined relaxation time for phonon scattering processes, calculated by $(\tau_C^i)^{-1} = (\tau_R^i)^{-1} + (\tau_N^i)^{-1}$. τ_R^i represents the relaxation time for all the phonon resistive scattering process and τ_N^i represents the relaxation time for phonon non-resistive scattering process (N process). For the phonon resistive scattering process, the Umklapp process scattering (U), boundary scattering (B), point defect scattering (PD), and resonant scattering (PR) are taken into consideration. Therefore,

$$(\tau_R^i)^{-1} = \sum_j (\tau_j^i)^{-1}, \quad j = U, B, PD, PR \quad (S6)$$

For the relaxation time of U-process, the expression proposed by Slack *et al.* was adopted:[5]

$$(\tau_U^i)^{-1} = B_U^i \left(\frac{k_B}{\hbar}\right)^2 x^2 T^3 e^{-\theta_i/3T}, \quad B_U^i \approx \frac{\hbar \gamma_i^2}{M v_i^2 \theta_i} \quad (S7)$$

Where M is average atomic mass and γ_i is the Grüneisen parameters of each phonon modes (set as fitting parameters).

For point defect scattering,[6, 7]

$$(\tau_{PD}^i)^{-1} = \frac{V k_B^4 \Gamma}{4\pi \hbar^4 v_i^3} x^4 T^4 \quad (S8)$$

Where V is average atomic volume, and Γ is the disorder parameter due to the mass fluctuation and strain fluctuation of the point defects which was set as a fitting parameter for the sake of simplicity.

For boundary scattering,

$$(\tau_B^i)^{-1} = \frac{v_i}{L} \quad (\text{S9})$$

Where L is the critical length of boundary scattering, also set as a fitting parameter for better accordance in very low temperature range.

For resonant phonon scattering,[8]

$$(\tau_{PR}^i)^{-1} = \frac{C_1 \omega^2}{(\omega_{o,1}^2 - \omega^2)^2} \quad (\text{S10})$$

Where $\omega_{o,1}$ is the resonance frequency of the oscillator and C_1 is the fitting parameters.

For N-process which was the least studied, we simply adopted the expression from the reference:[2]

$$(\tau_N^L)^{-1} = B_N^L \left(\frac{k_B}{\hbar}\right)^2 x^2 T^5, \quad B_N^L \approx \frac{k_B^3 v_L^2 V}{M \hbar^2 v_L^5} \quad (\text{S11a})$$

$$(\tau_N^T)^{-1} = B_N^T \left(\frac{k_B}{\hbar}\right) x T^5, \quad B_N^T \approx \frac{k_B^4 v_T^2 V}{M \hbar^3 v_T^5} \quad (\text{S11b})$$

The parameters used in the calculations are listed in Table S2.

Table S2. Physical parameters used in the modeling analysis

	Mg₃Sb₂	Mg₃Bi₂
$M/10^{-25}$ kg	1.05	1.63
$V/10^{-29}$ m ³	2.67	2.88
v_L/m	3794	3120
v_T/m	1984	1522
θ_L/K	378	303
θ_T/K	198	148
$\omega_{0,1}/\text{THz}$	8.33	5.80

Note: the sound velocity is from the experimental values[9]. The Debye temperature was calculated according to $\theta_i = \hbar v_i (6\pi^2 n)^{1/3} / k_B$, where n is the atom number in a unit volume. The resonant frequency is determined by the specific heat capacity.

Table S3. Fitting parameters for the modeling analysis

	Mg₃Sb₂	Mg₃Bi₂
L/mm	0.661	0.173
γ_L	4.33	6.49
γ_T	2.22	2.22
F	0.0152	0.0109
C_1/s^{-3}	3.68×10^{34}	5.27×10^{34}

References

- [1] J. Daniel Bryan, T. Henning, H. Birkedal, M. Christensen, V. I. Srdanov, H. Eckert, B. B. Iversen and G. D. Stucky, Magnetic phase diagram of Eu₄Ga₈Ge₁₆ by magnetic susceptibility, heat capacity, and Mössbauer measurements, Phys. Rev. B 68 (2003) 174429.
- [2] D. T. Morelli, J. P. Heremans and G. A. Slack, Estimation of the isotope effect on the lattice thermal conductivity of group IV and group III-V semiconductors, Phys. Rev. B 66 (2002) 195304.
- [3] J. Callaway, Low-Temperature Lattice Thermal Conductivity, Phys. Rev. 122 (1961) 787-790.

- [4] K. Biswas, J. He, Q. Zhang, G. Wang, C. Uher, V. P. Dravid and M. G. Kanatzidis, Strained endotaxial nanostructures with high thermoelectric figure of merit, *Nat. Chem.* 3 (2011) 160-166.
- [5] C. J. Glassbrenner and G. A. Slack, Thermal Conductivity of Silicon and Germanium from 3 K to the Melting Point, *Phys. Rev.* 134 (1964) A1058-A1069.
- [6] P. Klemens, The scattering of low-frequency lattice waves by static imperfections, *Proc. Phys. Soc. Sect. A* 68 (1955) 1113.
- [7] B. Abeles, Lattice Thermal Conductivity of Disordered Semiconductor Alloys at High Temperatures, *Phys. Rev.* 131 (1963) 1906-1911.
- [8] P. Ying, X. Li, Y. Wang, J. Yang, C. Fu, W. Zhang, X. Zhao and T. Zhu, Hierarchical Chemical Bonds Contributing to the Intrinsically Low Thermal Conductivity in α -MgAgSb Thermoelectric Materials, *Adv. Funct. Mater.* 27 (2017) 1604145.
- [9] W. Peng, G. Petretto, G.-M. Rignanese, G. Hautier and A. Zevalkink, An Unlikely Route to Low Lattice Thermal Conductivity: Small Atoms in a Simple Layered Structure, *Joule* 2 (2018) 1879-1893.